Chemical Engineering Journal 145 (2009) 362–370

Contents lists available at ScienceDirect

Chemical Engineering Journal

journal homepage: www.elsevier.com/locate/cej

Dynamics and control of solar thermochemical reactors

Jörg Petrasch [a,*], Philippe Osch [a], Aldo Steinfeld [a,b]

[a] Department of Mechanical and Process Engineering, ETH Zürich, 8092 Zürich, Switzerland
[b] Solar Technology Laboratory, Paul Scherrer Institute, 5232 Villigen, Switzerland

ARTICLE INFO

Article history:
Received 18 October 2007
Received in revised form 7 July 2008
Accepted 23 July 2008

Keywords:
Solar thermochemistry
Dynamics
Control
Gasification
Zinc cycle

ABSTRACT

A general dynamic model for solar-driven thermochemical processes is formulated based on unsteady mass and energy conservation equations coupled to the reaction kinetics. It is applied to two pertinent high-temperature thermochemical reactors for fuel production that make use of concentrated solar energy as the source of process heat, namely: an indirectly irradiated batch-operated packed bed reactor for the carbothermic reduction of zinc oxide, and a directly irradiated continuously operated particle flow reactor for the steam-gasification of petcoke. Model parameter identification and validation is accomplished by comparing numerically simulated and experimentally measured temperatures and outlet product concentrations. A linear feedback controller was implemented using the LQG/LTR design method. Simulations of the controlled reactor system with real solar irradiation data indicates improved quality and steadiness of product composition throughout transient solar input phases and superior solar-to-chemical energy conversion efficiency.

© 2008 Elsevier B.V. All rights reserved.

1. Introduction

Solar thermochemical processes, in which high-temperature process heat is exclusively supplied by concentrated solar energy, provide an efficient route for fuel and material production with significant avoidance of CO_2 emissions [1]. These processes are characterized by the intermittent nature of solar irradiation and, therefore, are inherently transient, especially during sunrise, sunset, and passing clouds. Thus, their dynamic behavior is critical for efficient and safe operation. Previous studies on dynamics and control of solar thermal systems include flat plate solar collectors [2–7], solar heating [8], solar air conditioning and refrigeration [9–11], solar heating in space applications [12], solar steam generation [13–17], solar furnace operation [18], and solar thermal power plants [19,20]. Widely used is the software package TRNSYS, which allows for dynamic simulation of conventional solar components and systems, but cannot handle solar thermochemical processes that involved coupled mass/heat transport of reactive flows. Dynamics of coupled solar chemical processes have been investigated for solar steam-reforming of methane [21], solar H_2 generation [22], and solar photochemical wastewater detoxification [23]. Reviews on process modeling and control are presented in Refs. [24–26].

This paper investigates the characteristic dynamic behavior of solar thermochemical reactors during the daily start-ups, shut-downs, and throughout cloudy conditions. It presents the formulation of a general non-linear dynamic modeling concept from first principles (i.e., mass and energy conservation) that is applicable to a wide range of solar chemical reactors. First-principles based models are chosen because they give additional insights into reactor dynamics and efficiency as well as into the behavior of scale-up reactors. Furthermore, they are less likely to give nonsensical results if applied under conditions significantly different from those used during parameter identification (graceful degradation).

Specifically, the model is applied to a solar reactor for carbothermal ZnO reduction [27] and to a solar reactor for solar thermal gasification of petcoke [28]. In addition, a process controller using feedforward and feedback control is developed aimed at ensuring the safe, stable, and efficient operation of solar chemical reactors during transients.

2. Dynamic model and process control

The reactor model structure is influenced primarily by the (i) irradiation mode (direct/ indirect irradiation of reactants), (ii) operational mode (batch/semi-batch/continuous feeding of reactants), and (iii) number of species and phases (solid/liquid/gas) [29]. Table 1 lists a classification of solar chemical reactors for the production of fuels and materials employed in experimental campaigns from 1990 onwards.

* Corresponding author.
E-mail address: j.petrasch@gmx.net (J. Petrasch).

1385-8947/$ – see front matter © 2008 Elsevier B.V. All rights reserved.
doi:10.1016/j.cej.2008.07.051

Nomenclature

A	Area (m^2)
$\bar{c}_{p,j}$	mole specific heat of species j at constant pressure (J/(K mol))
$c_{v,S}$	mass specific heat of solid S at constant volume (J/(K kg))
d	Layer thickness (m)
E_a	reaction activation energy (J/mol)
F_{k-j}	diffuse view factor between surface k and j
$\bar{h}_j$	mole specific enthalpy of species j (J/mol)
k	Thermal conductivity (W/(m K))
k_0	kinetic frequency factor
LQG/LTR	linear quadratic Gaussian with loop transfer recovery
m	mass (kg)
n	number of moles (mol)
$\dot{n}_j$	molar flow rate of species j (mol/s)
P	partial pressure (Pa)
PSI	Paul Scherrer Institute
$\dot{q}_j$	net radiative flux through surface j (W/m^2)
$\dot{Q}$	heat flow (W)
r_j	molar rate of formation/consumption of species j (mol/s)
RMS	root mean square
S	solid
R	ideal gas constant (J/(mol K))
t	time (s)
T	temperature (K)
$\vec{u}$	system input vector
U	overall heat transfer coefficient (W/K)
$\vec{x}$	system state vector
$\vec{y}$	system output vector
α	absorptivity
δ_{kj}	Kronecker delta ($\delta_{kj}=1$ for $k=j$ and $\delta_{kj}=0$ for $k \neq j$)
ε	emissivity
η	efficiency
σ	Stefan–Boltzmann constant, 5.67×10^{-8} W/(m^2 K^4)

Subscripts

aperture	aperture
app	apparent
in	inlet
j	counter for species; counter for enclosure surfaces
k	counter for enclosure surfaces
out	outlet
R	reaction site
s	solid
ss	steady state

2.1. Domain

Fig. 1 depicts the system domain, which features a well insulated cavity that absorbs concentrated solar radiation and uses it as the source of high-temperature process heat to drive an endothermic chemical reaction. Inputs are: solar power input Q^*_{solar}, reactant molar flow rates n^*_{in}, reactant pressure, temperature, and composition at the inlet. Outputs are: temperatures T, product molar flow rate n^*_{out}, product thermodynamic state, and product composition at the outlet. The methodology follows a lumped-parameter approach [46–48]. Only relevant dynamics parameters, i.e. those evolving on the same time scale as the output of interest, are considered. Model parameter identification and validation is performed by comparing numerically simulated and experimentally measured product flow rates, product concentrations, and reactor temperatures.

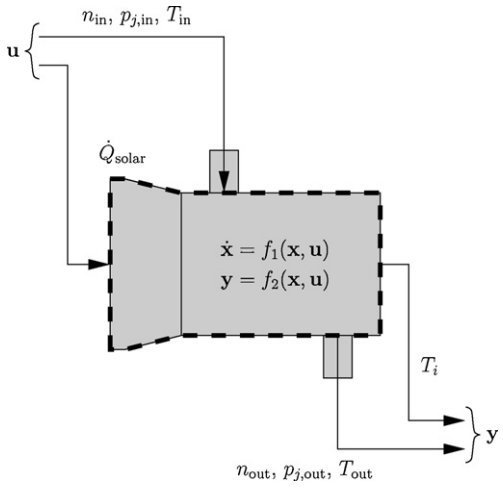

Fig. 1. Schematic of reactor domain boundaries (dotted line), input $\vec{u}$, output $\vec{y}$, and system state $\vec{x}$.

2.2. Mass conservation

Unsteady mass conservation for species undergoing a chemical transformation yields:

$$\frac{dn_j}{dt} = n^*_{j,in} - n^*_{j,out} + r_j \quad (1)$$

where the molar rate of formation/consumption of species j is given by its kinetic rate law,

$$r_j = \sum_{l=1}^{N} M_{j,l} k_l f_l(p_i) \quad (2)$$

With $M_{j,l}$ denoting the stoichiometric coefficient of species j in reaction l, and p_i ($i=1, \ldots, N_s$) denoting the partial pressure of species i, and k_l denoting the rate constant of reaction l:

$$k_l = k_0 \, e^{-E_{a,l}/RT_R} \quad (3)$$

The kinetic rate law expressions for the carbothermal reduction of ZnO and for the steam-gasification of petcoke gasification are taken from Refs. [49,50], respectively.

2.3. Energy conservation

Applying the unsteady energy conservation equation to a solid, no-reacting component S (e.g., a reactor wall), expressing the solid internal energy in terms of the solid temperature, and assuming constant specific heat, yields:

$$m_s c_s \frac{dT_s}{dt} = Q^*_{radiation,s} + Q^*_{convection,s} + Q^*_{conduction,s} \quad (4)$$

The net radiative heat power $\dot{Q}_{radiation}$ is given by the difference of the solar radiation absorbed and the thermal radiation re-radiated through the reactor's aperture of area $A_{aperture}$

$$Q^*_{radiation,s} = A_{aperture}(\alpha_{app} Q^*_{solar} - \varepsilon_{app} \sigma T_s^4) \quad (5)$$

where α_{app}, ε_{app} are the apparent absorptivity and emissivity of the solar reactor, respectively. For cavity-type geometries approaching blackbody absorbers, α_{app} and ε_{app} usually approach unity. During

Table 1
Classification of selected solar reactor designs for the production of fuels and materials, employed in experimental campaigns from 1990 onwards.

Application	Reference	Irradiation mode	Operational mode	Reaction[a]
CH_4 reforming	[30]	Direct	Continuous	g+g→g+g
CH_4 reforming	[31]	Direct	Semi-batch	g+g→g+g
CH_4 reforming	[32]	Indirect	Continuous	g+g→g+g
CH_4 reforming	[33]	Indirect	Continuous	g+g↔g+g
CH_4 cracking	[34]	Direct	Continuous	g→s+g
CH_4 cracking	[35]	Indirect	Continuous	g→s+g
C gasification	[28]	Direct	Continuous	s+g→g+g
$CaCO_3$ decomposition	[36]	Direct	Continuous	s→s+g
Fe_3O_4 reduction	[37]	Direct	Semi-batch	s→l+g
Ferrite reduction	[38]	Direct	Semi-batch	s→s+g
ZnO reduction	[39]	Direct	Semi-batch	s→g+g
CH_4 reforming/ZnO reduction	[40]	Direct	Continuous	s+g→g+g+g
ZnO reduction	[41]	Direct	Continuous	s→g+g
ZnO carbo-reduction	[42]	Indirect	Semi-batch	s+s→g+g
ZnO carbo-reduction	[27]	Indirect	Semi-batch	s+s→g+g
Fullerene synthesis	[43]	Direct	Continuous	s→g→s
Al melting	[44]	Direct	Batch	s→l
NH_3 dissociation	[45]	Indirect	Continuous	g↔g+g

[a] Simplified overall reaction; s, l, g: species in solid, liquid and gaseous phase.

parameter identification, α_{app} is a free parameter. For the secondary cavity (Fig. 3) the radiosity method [51] is applied to calculate heat exchange between the separating plate and the reaction site. Isothermal, gray, and diffuse surfaces are assumed.

$$\sum_{j=1}^{N}\left(\frac{\delta_{kj}}{\varepsilon_j}-F_{k-j}\frac{1-\varepsilon_j}{\varepsilon_j}\right)q_j=\sum_{j=1}^{N}F_{k-j}(T_k^4-T_j^4),\quad k=1,2 \tag{6}$$

where F_{k-j} denotes the view factor between surface k and j, $\dot{q}_j$ is the net radiative heat flux leaving surface j, and δ_{kj} is the Kronecker delta. The dynamics of convection heat transfer are relatively fast (timescale smaller than 10^{-1} s), as flow patterns adjust quickly to changes in surface temperatures. Hence, convection heat transfer is modeled as static. The reactor temperature is uniform due to mixing effects. Hence, conduction losses can be approximated by a static linear function of reactor temperature. Finally, a combined conduction–convection heat transfer coefficient UA is determined by parameter identification.

$$Q^*_{\text{convection,s}}+Q^*_{\text{conduction,s}}=\sum_k UA_{s-k}(T_k-T_s) \tag{7}$$

where T_k is the temperature of the adjacent reservoir (insulation or ambient temperature). Note that the time constant of a solid thermal conductor is proportional to its thermal capacity and inversely proportional to its thermal conductivity. As the thermal conductivity of insulation materials is inherently low, time scales of the insulation are relevant and insulation time constants have been calculated at up to 4.5×10^4 s [21]. The reaction chamber is modeled as a continuously stirred tank reactor (CSTR) [46,47], operating at constant atmospheric pressure. Typical pressure differences between inlet and outlet are low (on the order of several mbars). Neglecting pressure gradients and kinetic/potential energy effects, energy conservation at the reaction site yields:

$$\begin{aligned}\frac{dT_R}{dt}\sum_{\text{species},j}n_{j,R}\bar{C}_{p,j}=&\sum_{\text{species},j}n^*_{j,\text{in}}(\bar{h}(T_{\text{in}})-\bar{h}_j(T_R))\\&-\sum_{\text{species},j}r_j\bar{h}_j(T_R)-Q^*_{\text{radiation,R}}\\&+Q^*_{\text{convection,R}}+Q^*_{\text{conduction},R}\\&+Q^*_{\text{convection,R}}+Q^*_{\text{conduction,R}}\end{aligned} \tag{8}$$

where T_R is the reaction site temperature, and $Q^*_{\text{radiation,R}}$, $Q^*_{\text{convection,R}}$, and $Q^*_{\text{conduction,R}}$ are modeled analogously to the heat flows on a solid reactor component. Note that the first term on the RHS of Eq. (8) accounts for the enthalpy change by sensible/latent heat; the second term accounts for the enthalpy change by the reaction.

2.4. Process control

The process controller should ensure: (i) constant product composition throughout transients (i.e., good disturbance rejection), (ii) high energy conversion efficiency and product quality (i.e., good tracking of reference signal), and (iii) robustness against model and signal uncertainties (e.g., model inaccuracies, linearization errors, measurement noise, signal drift). The implemented control structure is shown in Fig. 2. Measured product composition and reaction temperature are fed to the controller; control action is taken over reactant mass flow rate. The design of a linear feedback controller follows the LQG/LTR method [52]. A supplementary feedforward channel is implemented to enhance controller response time. The signal gain K is tuned such that the RMS of the set-point deviation is minimized. The model and controller are implemented using MATLAB/Simulink; parameters are identified using MATLAB's build-in `fminsearch` function with the Nelder-Mead minimization algorithm. Radiative properties, thermal conductivities, and specific heats of reactor components are calculated using constant mean values [53,54]. Thermodynamic properties of reactants (ZnO, C, H_2O) and inert gases (Ar, N_2) are calculated using constant mean

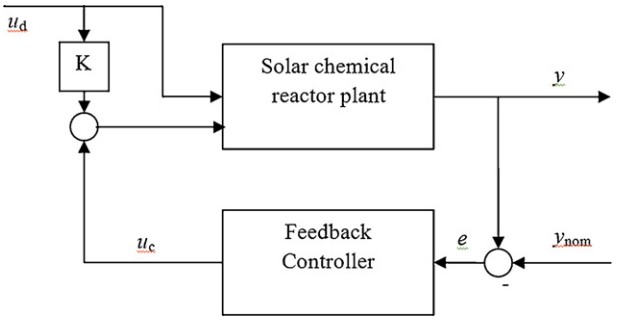

Fig. 2. Control structure with feedforward and feedback control. K is the gain, u_d is the disturbance input $\dot{Q}_{solar}$, e the control error, u_c the feedback controller output, and u_s the controller input to the plant.

values. Reaction enthalpies are calculated by first order approximations [55]. Numerical integration is performed by a Runge-Kutta based predictor/corrector scheme with variable step size.

3. Parameter identification and validation

The dynamic model is applied to two very distinctive solar reactors; (1) *Reactor 1* for carbothermal ZnO reduction [27] and; (2) *Reactor 2* for solar thermal gasification of petcoke [28].

3.1. Reactor 1

The solar reactor for the carbothermal reduction of ZnO is shown schematically in Fig. 3. It consists of two cavities in series, of which the upper one is functioning as the solar absorber and the lower one as the reaction chamber containing a ZnO/C packed bed [27,49]. The net reaction, represented by $ZnO + C = Zn(g) + CO(g)$, proceeds endothermically at reasonable rates at above 1300 K. Thus, this reactor belongs to the indirect-irradiation, batch-operation, $s + s \rightarrow g$ category. A 5 kW reactor prototype was experimentally investigated at PSI's high-flux solar furnace [56] in the 400–1600 K range. The kinetic rate law expression and the activation energy E_a of 201.5 kJ/mol are taken from Refs. [27,49]. The identified parameters and their final values are summarized in Table 2.

Heat transfer to the reactor wall is dominated by thermal radiation. At $T_R > 1500$ K, the rate of radiative heat transfer is much faster than that of conductive heat transfer through the insulation, as indicated by linearization of radiative heat transfer rate: $\sigma T_{R0}^3 >> 2k_{iso}/d_{iso}$. Note that reactor wall and insulation are modeled as a single reservoir. Thus, heat transfer to the insulation is

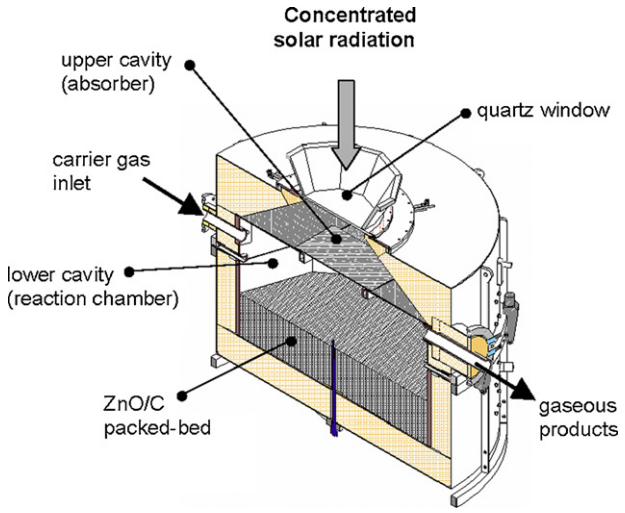

Fig. 3. Schematic of the solar chemical reactor, featuring two cavities in series with the upper one functioning as the solar absorber and the lower one as the reaction chamber containing a ZnO/C packed-bed [27].

Table 2
Identified model parameters of the solar reactor for the carbothermic reduction of ZnO.

Parameter (units)	Description	Value
m_R (kg)	Reactor batch mass	1.12
m_I (kg)	Insulation mass	4.82
m_{SP} (kg)	Separating plate mass	0.49
UA_l (W/K)	Lower cavity overall heat transfer coefficient	0.77
UA_u (W/K)	Upper cavity overall heat transfer coefficient	0.90
α_{app}	Apparent absorptivity	0.87
k_0 (mol/s)	Frequency factor	2.37×10^4

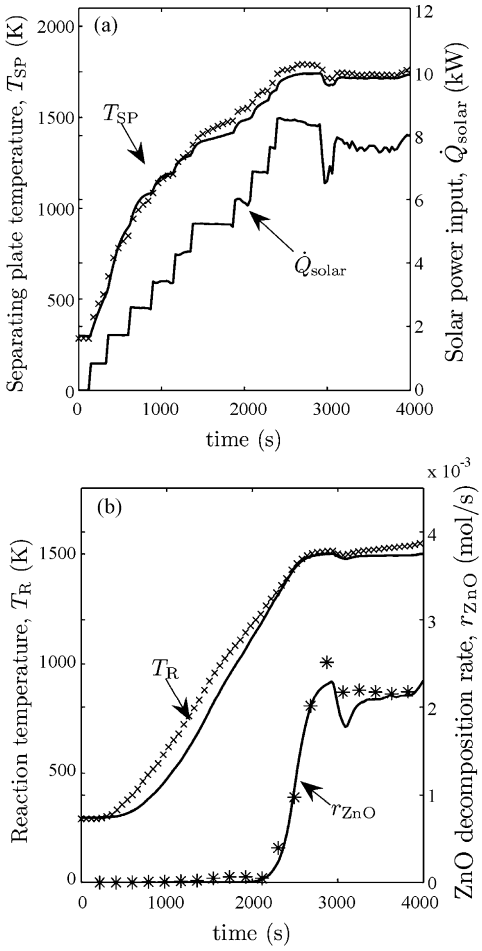

Fig. 4. Representative solar experimental run using the solar reactor for the carbothermic reduction of ZnO: (a) separating plate temperature T_{SP} and solar power input Q_{sol}; (b) reaction site temperature T_R and reaction rate. Data points are the experimentally measured values; solid curves are the numerically simulated values.

rate-controlled by conduction. The mean insulation thickness is $d = 0.08$ m, the surface area of the upper and lower cavities are $A_u = 0.05$ m^2 and $A_l = 0.08$ m^2, and the thermal conductivity of the porous insulation is $k = 0.3$ W/mK. Assuming steady-state conduction heat transfer in a 1-D plane layer, the UA obtained is in the range 0.4–0.6 W/K. As expected, the identified values 0.77 and 0.9 W/K for UA_l and UA_u, respectively, are higher than the steady state-based estimates since the temperature profile at the wall/insulation is steeper immediately after an external temperature change than in the steady state. Hence, heat transfer rates are higher during transients than in steady state.

Fig. 4 shows a representative solar experimental run and its comparison to the model prediction. Data points are the experimentally measured values from different set of experiments than used for parameter identification; curves are the numerically simulated ones. At $t = 0$, all components are at ambient temperature. The solar power input is increased stepwise to approximately 8 kW, while the reactor is constantly purged with N_2. The reaction proceeds at reasonable rates when the reaction site temperature T_R exceeds 1300 K. The agreement is reasonably good: the absolute RMS errors of the separating plate temperature T_{SP} and of the reaction site temperature T_R are 40.5 and 74.8 K, respectively. During heating, the simulated T_R deviates slightly from the measured one because of the lumped parameter assumption. The thermocouple measures a local temperature whereas the model

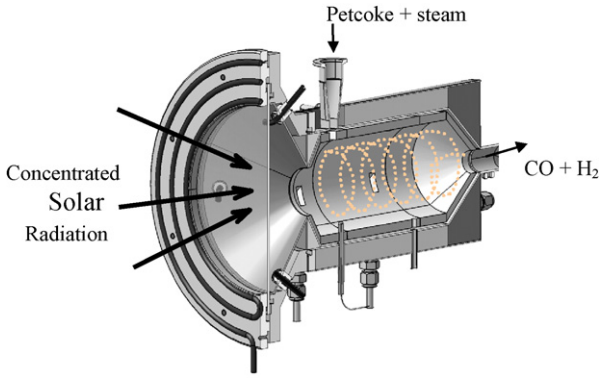

Fig. 5. Schematic of the solar chemical reactor for the steam-gasification of petcoke, featuring a continuous gas-particle vortex flow confined to a cavity receiver and directly exposed to concentrated solar radiation. The reactants are a mixture of steam and petcoke [28].

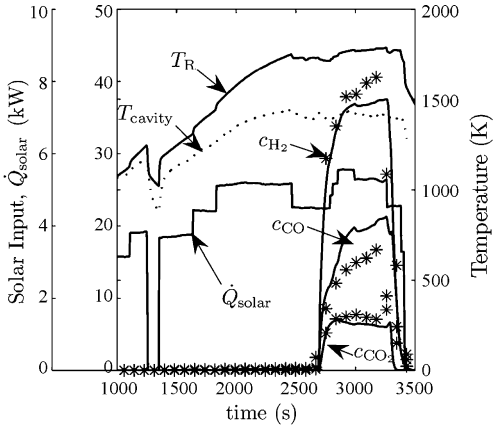

Fig. 6. Representative solar experimental run using the solar reactor for the steam-gasification of petcoke: reaction site and cavity wall temperatures, and product composition. Data points are the experimentally measured values; solid curves are the numerically simulated values.

predicts an overall packed-bed temperature. Further uncertainties are derived from the optical measurement of the solar power input.

3.2. Reactor 2

The solar reactor for the steam-gasification of petcoke is shown schematically in Fig. 5. It consists of a continuous flow of steam laden with petcoke particles, confined to a solar cavity-receiver and directly exposed to concentrated solar radiation [28]. The net reaction, represented by $C + H_2O = H_2 + CO$, proceeds endothermically at reasonable rates at above 1500 K. Thus, this reactor belongs to the direct-irradiation, continuous-operation, $s + g \rightarrow g$ category. A 5 kW reactor prototype was experimentally investigated at PSI's high-flux solar furnace [56]. The identified parameters and their final values are summarized in Table 3.

The identified value of the apparent absorptivity, α_{app}, is 0.94, which is consistent with the value calculated using the radiosity method for the cylindrical geometry of *Reactor 2* ([51], Table 6.1, p. 239). Similar to *Reactor 1*, heat transfer to the reactor wall is dominated by thermal radiation. At $T_R > 1500$ K, the rate controlling heat transfer mode in the insulation is conduction. The diameter of the inner Al_2O_3 porous insulation material layer is $d = 0.01$ m, the inner cavity surface area is $A = 0.08\ m^2$, and the thermal conductivity of the porous Al_2O_3 insulation is $k = 0.75\ W/(m^2K)$ at 800 K. Thus, assuming steady-state conduction heat transfer in a 1-D plane layer, the *UA* obtained is 12 W/K. As expected, the identified value of 20.7 W/K is higher than the estimate due to steep temperature profiles during transients.

Fig. 6 shows a representative solar experimental run and its comparison to the model prediction. Data points are experimentally measured values from a different set of experiments than used for parameter identification; curves are the numerically simulated ones. At $t = 0$, all components are at ambient temperature. Note that the measured nominal cavity wall temperature T_{cavity} is significantly lower than the simulated reaction site temperature T_R because the direct irradiation of the gas-particle flow provides an efficient means of heat transfer directly to the reaction site and, simultaneously, the particle cloud serves as a radiation shield to the cavity walls [57]. During heating, the reactor is subjected to concentrated solar power while purged with Ar. Steam-petcoke mixture is injected $t = 2750$ s. At $t = 3500$ s, solar power input and reactant injection are stopped. The agreement is reasonably good: the average absolute RMS error of the product concentrations is 2.0%. Deviations are attributed to inaccuracies derived from the solar power input measurement and from the low sampling rate of the gas chromatograph used for measuring the product gas composition downstream of the reactor.

Table 3
Identified model parameters of the solar reactor for the steam-gasification of petcoke.

Parameter (units)	Description	Value
m_I (kg)	Insulation mass	2.01
UA (W/K)	Overall heat transfer coefficient	20.7
n_{tot} (mol)	Molar reactor content	0.49
m_C (g)	Petcoke mass	0.02
α_{app}	Apparent absorptivity	0.94

3.3. Energy conversion efficiency analysis

The following cases are simulated: (i) an idealized sunny day, (ii) a real sunny day, and (iii) a real partly cloudy day. Solar irradiation measurements from the Solar Radiation Research Laboratory of the National Renewable Energy Laboratory (NREL; US) are used [58]. Initially, all temperatures are at ambient. For the carbothermic reduction of ZnO (*Reactor 1*, Fig. 3), the reaction starts autonomously as the temperature increases. For the steam-gasification of petcoke (*Reactor 2*, Fig. 5), the feeding of the reactants starts at $t = 2750$ s. The overall solar-to-chemical energy conversion efficiency is defined as:

$$\eta(t) = \frac{\int_0^t (\sum_j (n^*_{out}(t') y_{j,out}(t') - n^*_{in}(t') y_{j,in}(t')))\, dt'}{\int_0^t Q^*_{solar}\, dt'} \tag{9}$$

At steady state,

$$\eta_{ss} = \frac{\sum_j (n^*_{out} y_{j,out} - n^*_{in} y_{j,in}) |_0 \overline{h_j}(T_R)}{Q^*_{solar}} \tag{10}$$

The relative difference between the overall and steady-state efficiency at the end of the day is:

$$\Delta\eta = \frac{\eta_{ss} - \eta(t = t_{final})}{\eta} \tag{11}$$

Fig. 7 shows the variation of the solar-to-chemical energy conversion efficiency during 3 simulated solar runs: (a) idealized sunny day, (b) real sunny day, and (c) partly cloudy day, for both solar reac-

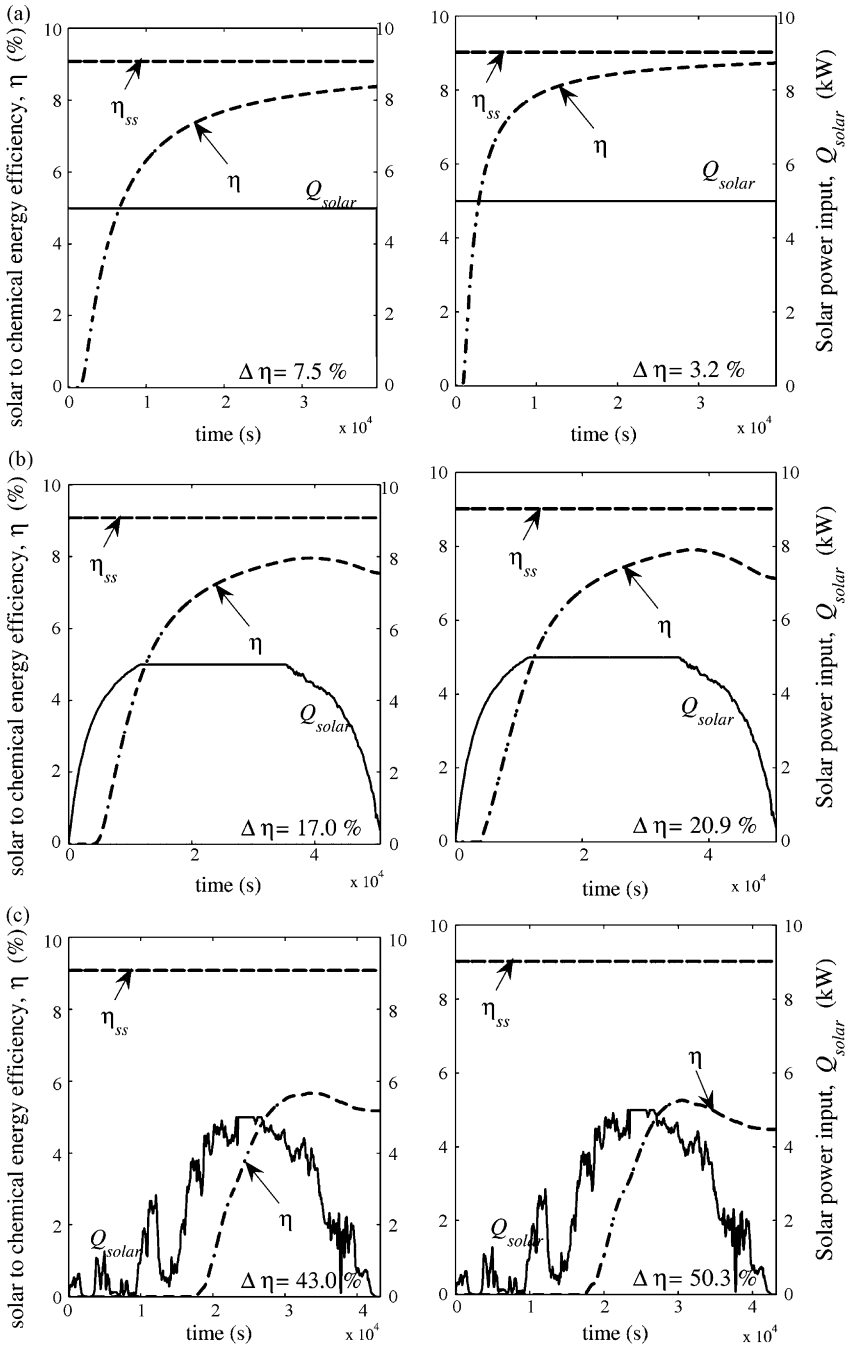

Fig. 7. Variation of the solar-to-chemical energy conversion efficiency during simulated solar runs: (a) Idealized sunny day, (b) real sunny day; (c) partly cloudy day. *Left*: *Reactor 1* for the solar carbothermic reduction of ZnO. *Right*: *Reactor 2* for the solar steam-gasification of petcoke.

tors (*left*: reactor 1 for the carbothermic reduction of ZnO; r*ight*: reactor 2 for the steam-gasification of petcoke). For case (a), a constant solar power input of 5 kW during 11 h is employed. As the day progresses, efficiency losses during the heating phase are compensated while η converges towards η_{ss}. Reactor 1 exhibits slower convergence due to its higher thermal inertia, caused by an additional separating plate and massive insulation ($\Delta\eta_{\text{reactor 1}} = 7.5\%$, $\Delta\eta_{\text{reactor 2}} = 3.2\%$). For case (b), a representative irradiation profile of a perfectly cloudless day is employed. Solar input is limited to the nominal reactor power of 5 kW. In contrast to case (a), $\Delta\eta_{\text{reactor 1}} > \Delta\eta_{\text{reactor 2}}$, because, during phases of low solar irradiation, temperatures are not high enough for the carbothermic reaction to proceed at reasonable rates. While *Reactor 1* is able to store thermal energy in components of high thermal capacitance, *Reactor 2* rapidly reaches steady state but can only store little energy. For case (c), an irradiation profile of a representative partly cloudy day is employed. Thermal inertia leads to a reduced η due to longer heating phases, but this effect can be alleviated when using the relatively low solar power input during sunrise and sunset for preheating purposes. η at the end of the day is only half of the maximum achievable efficiency. The thermal inertia effect is expected to become more pronounced for scaled-up reactors due to their higher mass and relatively smaller heat losses. Insulating the reactor aperture during night time may reduce heat-up time in the morning as the reactor will retain a relatively high temperature overnight.

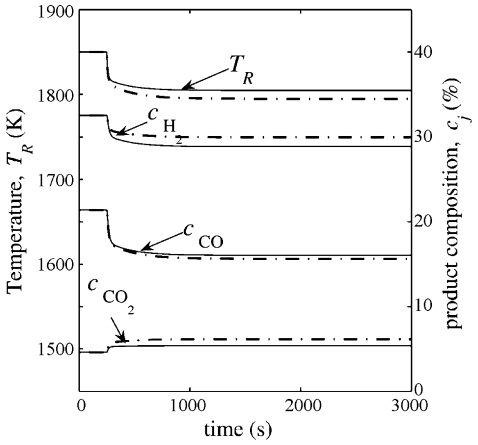

Fig. 8. Linear (dashed curve) and nonlinear (solid curve) response of the reaction site temperature and product composition to a 10% decrease in $\dot{Q}_{solar}$, for the scale-up version of *Reactor 2* for the steam-gasification of petcoke.

4. Controlled system

The dynamic nonlinear model is further developed for a scale-up version of *Reactor 2* (steam-gasification of petcoke) for a solar power input of 500 kW [28]. Surfaces are assumed to scale linearly with the input power, volumes are assumed to scale with $A^{3/2}$, the mean heat transfer coefficient U remains constant. To facilitate controller design, the model is linearized around the nominal operating point. Fig. 8 shows a comparison between the linear (dashed curve) and nonlinear (solid curve) response of the reaction site temperature and product composition to a 10% decrease in $\dot{Q}_{solar}$ from 500 to 450 kW. The relative difference remains below 14.8% for all output variables. Noticeable nonlinearities are the T^4 dependence of the radiation term and the $e^{-1/T}$ dependence of the kinetic rate term. The linear model analysis [52], shows that the model is stable, fully controllable, and fully observable. A model based linear quadratic Gaussian regulator with loop transfer recovery (LQG/LTR) is implemented as controller. Fig. 9 shows a comparison between controlled (using controller of Fig. 2) and uncontrolled systems. The reactor is first heated at constant $\dot{Q}_{solar} = 500$ kW. In the period between 3000 and 6000 s, a 15% decrease in $\dot{Q}_{solar}$ is simulated. Consequently, the controller decreases the steam inlet flow rate in such a way as to keep the CO_2 outlet concentration at constant low level. Simultaneously, T_R is maintained at a high level to ensure favorable chemical kinetics. Fig. 10 shows the sunrise-to-sunset simulation for a real, partly cloudy day (see Fig. 7c). The controller is switched on when the solar power input reaches 80% of its nominal value. For the uncontrolled reactor, CO_2 concentration increases with decreasing $\dot{Q}_{solar}$ (i.e. decreasing T_R). For the controlled reactor, the steam mass flow rate is adjusted to match the actual solar irradiation, resulting in a constant low CO_2 concen-

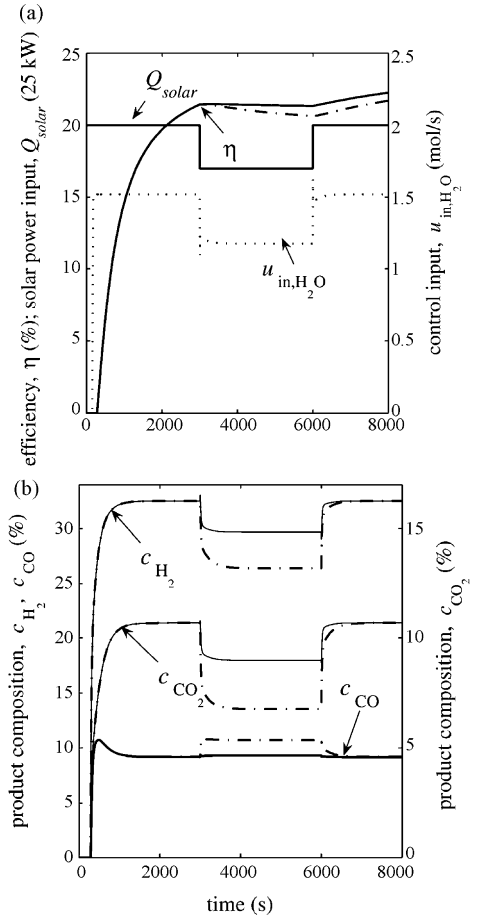

Fig. 9. Controlled (solid curve) and uncontrolled (dashed) system response to a 15% decrease in $\dot{Q}_{solar}$: (a) solar power input, steam inlet flow and solar-to-chemical energy conversion efficiency; (b) product outlet concentrations. The system is the scale-up version of *Reactor 2* for the steam-gasification of petcoke.

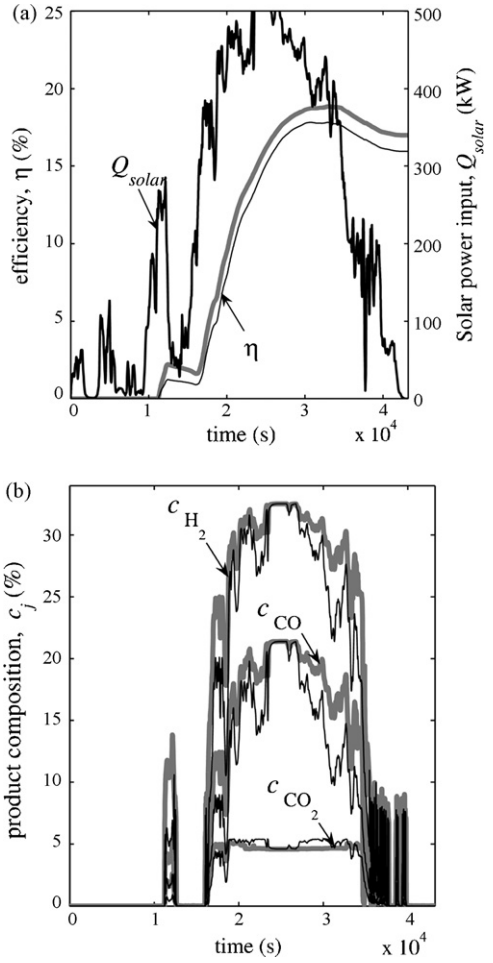

Fig. 10. Controlled (thick gray curves) uncontrolled (thin black curves) system simulation for a representative partly cloudy day: (a) solar power input and solar-to-chemical energy conversion efficiency; (b) product outlet concentrations. The system is the scale-up version of *Reactor 2* for the steam-gasification of petcoke.

tration in the product and, consequently, high syngas quality. The generally higher temperature level of the controlled system leads to faster reaction kinetics and, hence, increased efficiency. At the end of the day, η reaches 16.1 and 17.1% for the uncontrolled and controlled reactors, respectively. Thus, constant high quality of the reaction products and superior energy conversion efficiency can be obtained with a process control system throughout transient operating conditions.

5. Summary and conclusions

A general, low-order dynamic model was develop for solar thermochemical processes and applied for 2 specific solar reactors: an indirectly irradiated batch-operation packed-bed reactor for the carbothermic reduction of ZnO, and a directly irradiated continuous-operation particle flow reactor for the steam-gasification of petcoke. Model parameters were determined by static and dynamic identification, and the identified models were validated with solar experimental runs. It was found that higher thermal inertia leads to lower solar-to-chemical energy conversion efficiency, but phases of relatively low solar irradiation (sunrise, sunset, clouds) can be used for preheating purposes. A model-based linear feedback LQG/LTR controller was designed for the scaled-up version of the solar reactor. The controller was supplemented with a feedforward channel, anticipating system behavior and enhancing controller response time. For a real day simulation of the controlled system, the overall efficiency was improved by 6.2% vis-à-vis that of the uncontrolled system.

Acknowledgements

We thank C. Wieckert from the Paul Scherrer Institute and A. Z'Graggen and D. Trommer from ETH Zurich for providing the solar experimental data.

References

[1] A. Steinfeld, A. Meier, Solar fuels and materials, in: Encyclopedia of Energy, Elsevier Science, 2004.
[2] A. Deron, Dynamic modeling and verification of a flat-plate solar collector, Solar Energy 24 (1980) 117n–128n.
[3] M. Hashish, M. El-Refaie, Reduced order dynamic model of the flat-plate solar collector, Appl. Math. Modell. 7 (1983).
[4] C. Jallut, A. Jemni, M. Lallemand, Steady-state and dynamic characterization of an array of flat-plate collectors, Solar Wind Technol. 5 (1988) 573–579.
[5] E. Arinze, G. Schoenau, S. Sokhansanj, S. Adefila, S. Mumah, A dynamic performance simulation model of flat-plate solar collectors for a heat pump system, Energy Convers. Manage. 34 (1993) 33–49.
[6] M. Chaabenen, M. Annabi, A dynamic model for predicting solar plant performance and optimum control, Energy 22 (1997) 567–578.
[7] J. Buzas, I. Farkas, A. Biro, R. Nemeth, Modelling and simulation aspects of a solar hot water system, Math. Comput. Simul. 48 (1998) 33–46.
[8] M. Al-Nimr, R. Damseh, Dynamic behaviour of baffled solar air heaters, Renewable Energy 13 (1998) 153–163.
[9] N. Le Perriès, N. Mazet, D. Stitou, Modeling and performances of a deep-freezing process using low grade solar heat, Energy 32 (2007) 154–164.
[10] S. Kaushik, S. Rao, R. Kumari, Dynamic simulation of an aqua-ammonia absorption cooling system with refrigerant storage, Energy Convers. Manage. 32 (1991) 197–206.
[11] S. Kaushik, N. Sheridan, K. Lam, S. Kaul, Dynamic simulation of an ammonia-water absorption cycle solar heat pump with integral refrigerant storage, Heat Recov. Syst. 5 (1985) 101–116.
[12] H. Cui, X. Hou, X. Yuan, Energy analysis of space solar dynamic heat receivers, Solar Energy 74 (2003) 303–308.
[13] D. Sworder, R. Rogers, An LQ-solution to a control problem associated with a solar thermal central receiver, IEEE Trans. Automat. Control 28 (10) (1983) 971–978.
[14] A. Ray, Dynamic modeling of once-through subcritical steam generation for solar applications, Appl. Math. Modell. 4 (1980).
[15] A. Ray, Nonlinear dynamic model of a solar steam generator, Solar Energy 26 (1981) 297–306.
[16] C. Maffezzoni, F. Parigi, Dynamic analysis and control of a solar power plant - II control system design and simulation, Solar Energy 28 (1982) 117–128.
[17] C. Maffezzoni, F. Parigi, Dynamic analysis and control of a solar power plant—I dynamic analysis and operation criteria, Solar Energy 28 (105–116) (1982).
[18] M. Berenguel, E.F. Camacho, F.J. Garcia-Martin, F.R. Rubio, Temperature control of a solar furnace, IEEE Control Syst. Mag. 19 (1) (1999) 8–24.
[19] F.R. Rubio, M. Berenguel, E.F. Camacho, Fuzzy logic control of a solar power plant, IEEE Trans. Fuzzy Syst. 3 (4) (1995) 459–468.
[20] E.F. Camacho, M. Berenguel, Robust adaptive model predictive control of a solar plant with bounded uncertainties, Int. J. Adaptive Control Signal Process. 11 (4) (1997) 311–325.
[21] J. Petrasch, A. Steinfeld, Dynamics of a solar thermochemical reactor for steam-reforming of methane, Chem. Eng. Sci. 62 (15–16) (2007) 4214–4228.
[22] J. Dersch, A. Mathijssen, M. Roeb, C. Sattler, Modeling of a solar thermal reactor for hydrogen generation, in: Proceedings of the 5th International Modelica Conference, Vienna, September 4–5, 2006.
[23] J.D. Alvarez, W. Gernjak, S. Malato, M. Berenguel, M. Fuerhacker, L.J. Yebra, Dynamic models for hydrogen peroxide control in solar photo-fenton systems, Chem. Eng. J. 129 (2007) 37–44.
[24] B.W. Bequette, Nonlinear control of chemical processes: A review, Ind. Eng. Chem. Res. 30 (1991) 1391–1413.
[25] A.V. Sapre, J.R. Katzer, Core of chemical reaction engineering: One industrial view, Ind. Eng. Chem. Res. 34 (1995) 2202–2225.
[26] Y.S. Matros, Mathematical modeling of chemical reactors—Developement and implementation of novel technologies, Angew. Chem. Int. Ed. Engl. 29 (1990) 1235–1245.
[27] S. Kräupl, U. Frommherz, C. Wieckert, Solar carbothermic reduction of ZnO in a two-cavity reactor, J. Solar Energy Eng. 128 (2006) 8–15.
[28] A. Z'graggen, P. Haueter, D. Trommer, M. Romero, J.C. De Jesus, A. Steinfeld, Hydrogen production by steam gasification of petroleum coke using concentrated solar power—II. Reactor design, testing and modeling, Int. J. Hydrogen Energy 31 (2005) 797–811.
[29] O. Levenspiel, Chemical Reaction Engineering, vol. 3, John Wiley & Sons, New York, 1999.
[30] R. Buck, M. Abele, H. Baur, A. Seitz, R. Tamme, Developement of a volumetric receiver-reactor for solar methane reforming, J. Solar Energy Eng. 116 (1994) 449.
[31] T. Kodama, T.T. Shimizu, T. Satoh, M. Nakata, K.I. Shimizu, Stepwise production of CO-rich Syngas and hydrogen via solar methane reforming by using Ni(II)-ferrite redox system, Solar Energy 73 (2002) 363–374.
[32] M. Epstein, I. Spiewak, A. Segal, I. Levy, D. Liebermann, M. Meri, V. Lerer, Solar experiments with a tubular reformer, in: 8th International Symposium on Solar Thermal Concentrating Technologies, 1996.
[33] M. Levy, R. Levitan, E. Meirowitch, A. Segal, H. Rosin, R. Rubin, Chemical reactions in a solar furnace 2: direct heating of a vertical reactor in an insulated receiver. Experiments and computer simulations, Solar Energy 48 (1992) 395–402.
[34] A. Meier, V.A. Kirillov, G.G. Kuvshinov, Y.I. Mogilnykh, A. Reller, A. Steinfeld, Solar thermal decomposition of hydrocarbons and carbon monoxide for the production catalytic filamentous carbon, Chem. Eng. Sci. 54 (1999) 3341–3348.
[35] A.W. Weimer, J. Dahl, K. Büchler, A. Lewandowski, R. Pitts, C. Bingham, G.C. Glatzmaier, Thermal dissociation of methane using a solar coupled aerosol flow reactor, in: DOE Hydrogen Energy Review, 2001.
[36] A. Meier, E. Bonaldi, G.M. Cella, W. Lipinski, D. Wuillemin, Solar chemical reactor technology for industrial production of lime, Solar Energy 80 (2006) 1355–1362.
[37] P. Charvin, S. Abanades, G. Flamant, F. Lemort, Two-step water splitting thermochemical cycle based on iron oxide redox pair for solar hydrogen production, Energy 32 (2007) 1124–1133.
[38] M. Roeb, C. Sattler, R. Klüser, N. Monnerie, L. De Oliveira, A.G. Konstandopoulos, C. Agraphiotis, V.T. Zaspalis, L. Nalbandian, A. Steele, P. Stobbe, Solar hydrogen production by a two-step cycle based on mixed iron oxides, Solar Energy Eng. 128 (2006) 125–133.
[39] P. Haueter, S. Moeller, R. Paulumbo, A. Steinfeld, The production of zinc by thermal dissociation of zinc oxide, Solar Energy 67 (1999) 161–167.
[40] A. Steinfeld, S. Kräupl, Experimental investigation of a vortex-flow solar chemical reactor for the combined ZnO reduction and CH_4 reforming, J. Solar Energy Eng. 123 (2001) 237–243.
[41] S. Möller, R. Palumbo, The developement of a solar chemical reactor for the direct thermal dissociation of zinc oxide, J. Solar Energy Eng. 123 (2001) 83–90.
[42] R. Adinberg, M. Epstein, Experimental study of solar reactors for carboreduction of zinc oxide, Energy 29 (2004) 771–787.
[43] G. Flamant, J. Robert, S. Marty, J. Gineste, J. Giral, B. Rivoire, D. Laplaze, Solar reactor scaling-up: the fullerene case study, Energy 29 (2004) 801–809.
[44] K. Funken, M. Roeb, P. Schwarzboezl, H. Warnecke, Aluminum remelting using directly solar-heated rotary kilns, J. Solar Energy Eng. 123 (2001) 117–124.
[45] H. Kreetz, K. Lovegrove, A. Liuzzi, A solar-driven, ammonia-based thermochemical energy storage system, Solar Energy 67 (1999) 309–316.
[46] B.W. Bequette, Process Dynamics Modeling, Analysis and Simulation, Prentice Hall, 1998.
[47] B.W. Bequette, Process Dynamics Modeling, Analysis and Simulation, Prentice Hall, 2003.
[48] L. Guzzella, System Dynamics, Lecture notes, ETH Zürich, 2004.
[49] T. Osinga, G. Olalde, A. Steinfeld, Solar carbothermal reduction of ZnO: Shrinking packed-bed reactor modeling and experimental validation, Ind. Eng. Chem. Res. 43 (2004) 7981–7988.

[50] D. Trommer, DISS. no. 16784, Thermodynamic and kinetic analyses of the solar thermal gasification of petroleum coke, ETH, 2006.
[51] R. Siegel, J. Howell, Thermal Radiation Heat Transfer, vol. 4, Taylor & Francis, New York/London, 2002.
[52] S. Skogestad, I. Postlethwaite, Multivariable Feedback Control, John Wiley & Sons, New York, 2004.
[53] Insultech ReSiC materials datasheet, Insultech (www.insultech.ch), 2002.
[54] Insultech Insulform materials datasheet, Insultech (www.insultech.ch), 2002.
[55] HSC chemistry 5, Outokumpu Research Oy., 2002.
[56] P. Haueter, T. Seitz, A. Steinfeld, A new high-flux solar furnace for high-temperature thermochemical research, J. Solar Energy Eng. 121 (1999) 77–80.
[57] A. Z'graggen, A. Steinfeld, A two-phase reactor model for the steam-gasification of carbonaceous materials under concentrated thermal radiation, Chem. Eng. Process. 47 (4) (2008) 655–662.
[58] http://www.nrel.gov/midc/srrl%5Fbms/.